Melting phase relations in the systems Mg$_2$SiO$_4$-H$_2$O and MgSiO$_3$-H$_2$O and the formation of hydrous melts in the upper mantle

Davide Novella [a,b,c*], David Dolejš [d,e], Robert Myhill [a,f], Martha G. Pamato [a,g], Geeth Manthilake [a,b] and Daniel J. Frost [b]

[a] Bayerisches Geoinstitut, Universität Bayreuth, Universitätsstrasse 30, D-95447 Bayreuth, Germany

[b] Laboratoire Magmas et Volcans, Université Blaise Pascal, 5 Rue Kessler, 63038 Clermont-Ferrand, France

[c] Lawrence Livermore National Laboratory, Livermore, California 94550, USA

[d] Institute of Petrology and Structural Geology, Charles University, Albertov 6, CZ-12843 Praha 2, Czech Republic

[e] Present address: Institute of Earth and Environmental Sciences Albert-Ludwigs-University of Freiburg, Albertstrasse 23b, D-79104, Freiburg, Germany

[f] Present address: School of Earth Sciences, University of Bristol, Queens Road, BS8 1RJ, Bristol, UK

[g] Present address: Department of Earth Sciences, University College London, Gower Street, WC1E 6BT, London, UK

[*] Corresponding author. E-mail: dn345@cam.ac.uk; Tel: +44 1223 768327

Present address: Department of Earth Sciences, University of Cambridge, Downing Street, CB2 3EQ, Cambridge, UK

24 **Abstract**

25 High-pressure and high-temperature melting experiments were conducted in the systems

26 Mg_2SiO_4-H_2O and $MgSiO_3$-H_2O at 6 and 13 GPa and between 1150 to 1900 °C in order

27 to investigate the effect of H_2O on melting relations of forsterite and enstatite. The

28 liquidus curves in both binary systems were constrained and the experimental results

29 were interpreted using a thermodynamic model based on the homogeneous melt

30 speciation equilibrium, $H_2O + O^{2-} = 2\ OH^-$, where water in the melt is present as both

31 molecular H_2O and OH^- groups bonded to silicate polyhedra. The liquidus depression as a

32 function of melt H_2O concentration is predicted using a cryoscopic equation with the

33 experimental data being reproduced by adjusting the water speciation equilibrium

34 constant. Application of this model reveals that in hydrous $MgSiO_3$ melts at 6 and 13 GPa

35 and in hydrous Mg_2SiO_4 melts at 6 GPa, water mainly dissociates into OH^- groups in the

36 melt structure. A temperature dependent equilibrium constant is necessary to reproduce

37 the data, however, implying that molecular H_2O becomes more important in the melt with

38 decreasing temperature. The data for hydrous forsterite melting at 13 GPa are

39 inconclusive due to uncertainties in the anhydrous melting temperature at these

40 conditions. When applied to results on natural peridotite melt systems at similar

41 conditions, the same model infers the presence mainly of molecular H_2O, implying a

42 significant difference in physiochemical behavior between simple and complex hydrous

43 melt systems. As pressures increase along a typical adiabat towards the base of the upper

44 mantle, both simple and complex melting results imply that a hydrous melt fraction

45 would decrease, given a fixed mantle H_2O content. Consequently, the effect of pressure

46 on the depression of melting due to H_2O could not cause an increase in the proportion,

47 and hence seismic visibility, of melts towards the base of the upper mantle.

48

49 **Keywords:** olivine, enstatite, phase equilibria, hydrous melting, cryoscopic equation,

50 water speciation.

51

52 **1. Introduction**

53 The effect of H_2O on the formation of silicate melts underlies a number of igneous

54 processes taking place within the Earth's mantle. H_2O has an important influence on the

55 generation of magmas at subduction zones being both a metasomatic agent of the arc

56 magma source region and responsible for the high degrees of melting that produce these

57 magmas (e.g. Tatsumi et al., 1986). The lithospheric mantle shows abundant evidence for

58 metasomatism by H_2O-bearing melts (e.g. Menzies and Hawkesworth, 1987; Erlank et al.

59 1987) and several exotic magma types such as kimberlites and lamproites are likely

60 formed, at least in part, as a result of H_2O lowering the mantle solidus (e.g. Kushiro et al.,

61 1968; Kawamoto and Holloway, 1997; Sokol et al., 2013). H_2O induced melting of the

62 deep mantle has also been proposed to explain a number of geophysical observations

63 such as the Earth's seismic low velocity zone (Lambert and Wyllie, 1970; Mierdel et al.,

64 2007) and possible low velocity layers present on top of the transition zone (Tauzin et al.,

65 2010) and immediately below it (Schmandt et al., 2014). Recently, it was proposed that

66 H_2O-induced melts would tend to migrate in the lower mantle, and transfer H_2O from

67 ultramafic to mafic lithologies, as a result of the difference in H_2O storage capacities of

68 these rock types (Pamato et al., 2015).

69

In order to understand the production of hydrous melts in the Earth's mantle it is important to constrain how H_2O affects the melting behaviour of mantle materials. In this regard, a number of studies have been performed to quantify the effects of H_2O on lowering melting temperatures and increasing melt yields in natural mantle rock systems (Mysen and Boettcher, 1975; Hirose and Kawamoto, 1995; Gaetani and Grove, 1998; Balta et al., 2011; Tenner et al., 2012b; Novella et al., 2014). Determining the effect of H_2O on melting in natural chemical systems is challenging, however, due to the large number of chemical components that are potentially influenced by H_2O. These determinations are further complicated by a number of other instrumental factors, such as control of oxygen fugacity, attainment of equilibrium, H_2O and FeO loss from experimental capsules and the difficulty in determining the H_2O contents of melts (Brooker et al., 1998; Liu et al., 2006; Tenner et al., 2012b; Novella and Frost, 2014).

82

It has long been appreciated that the effects of H_2O on silicate melts can be more easily quantified by examining melting behavior in simple systems (Kushiro et al, 1968; Kushiro and Yoder, 1969; Kushiro, 1972; Hodges, 1973, 1974). From results of experiments in simple systems such as Mg_2SiO_4-SiO_2-H_2O, Kushiro (1972) proposed, for example, that hydrous mantle partial melts would be more SiO_2-rich compared to dry melts. Studies in simple systems can also be used to quantify the effect of H_2O on mineral melting at high pressures and experiments have been performed up to conditions equivalent to those in the mantle transition zone (Kushiro and Yoder, 1969; Luth, 1993; Inoue, 1994). While relatively detailed melting phase relations on hydrous forsterite

92   (Kushiro and Yoder, 1969; Hodges 1973) and enstatite (Kushiro and Yoder, 1969;

93   Kushiro et al., 1968) exist up to 3 GPa, phase relations at higher pressures are more

94   sparse and show less mutual agreement. Luth (1993) and Inoue (1994) investigated the

95   melting behavior of forsterite with 17-20 wt% H_2O up to pressures of 12 and 15.5 GPa,

96   respectively, although the two studies are in poor agreement. In addition, Inoue (1994)

97   also studied the phase relations of hydrous enstatite and an intermediate Mg/Si ratio

98   composition to similar pressures. However, in this previous study more emphasis was

99   placed on determining the conditions of the hydrous solidus rather than quantifying the

100   effect of melt H_2O content on the melting temperature.

101

102   Recently, several studies on natural multicomponent systems have proposed generalized

103   models for the effects of H_2O on peridotite melting temperatures (Medard and Grove,

104   2008; Tenner et al., 2012a). While such models are quite successful in reproducing the

105   experimental observations, they make assumptions concerning both the thermodynamic

106   data and the mechanism by which H_2O dissolves in melts that can be more easily tested

107   using results on simplified systems. In simplified systems additional constraints are also

108   provided by calorimetric measurements such as those performed to determine the entropy

109   of melting (Bottinga, 1985; Navrotsky et al., 1989; Richet et al., 1993; Tangeman et al.,

110   2001). One advantage of examining experiments in simple systems is that treatment with

111   relatively simple thermodynamic models should provide a firmer basis for understanding

112   hydrous melting on a physicochemical level (Burnham, 1975; Silver and Stolper, 1985)

113   and can be used to examine how the effect of H_2O on melting may be further modified by

114   pressure.

115

The goal of this study is to determine the melting phase relations in the systems

Mg_2SiO_4-H_2O and $MgSiO_3$-H_2O at upper mantle conditions. In particular, we investigate

the H_2O contents of melts in equilibrium with forsterite and/or enstatite as a function of

temperature at high pressure by bracketing the location of the hydrous liquidus curves.

The experimental data are analysed using thermodynamic models to provide insight into

the H_2O dissolution mechanism and its effects at high pressures. Results are presented for

both systems at 6 and 13 GPa corresponding to ~180 and ~390 km depth in the mantle,

and temperatures ranging between 1150 to 1900 °C.

124

2. Experimental and analytical details

Two sets of compositions were prepared for experiments in the systems Mg_2SiO_4-H_2O

and $MgSiO_3$-H_2O. In the system Mg_2SiO_4-H_2O, starting compositions were mixed from

two end-member compositions: Mg_2SiO_4 (forsterite) synthesized from high purity oxides,

MgO and SiO_2, and a 2:1 molar mixture of $Mg(OH)_2$ (brucite) and SiO_2. The pure

forsterite was synthesized by firing the oxides at 1500 °C for 2 hours and then grinding

the sintered mix for 1 hour under ethanol. This firing and grinding process was repeated 4

times. The 2:1 brucite-silica mixture corresponds to a composition of Mg_2SiO_4 with 20.4

wt% H_2O in the bulk. In order to prepare this end member, brucite and SiO_2 were dried

overnight at 120 °C and 1000 °C, respectively. The calculated amount of each component

was then weighed, ground for 1 hour under ethanol and dried under an infrared lamp. By

varying the mass proportions of the end member compositions a range of mixtures were

prepared with variable H_2O content but with a constant stoichiometry of Mg/Si= 2 (Table

138   1). All mixtures with water contents less than 20.4 wt% were prepared by grinding the

139   weighed proportions of dry forsterite and forsterite with 20.4 wt% bulk H_2O for 30

140   minutes under ethanol, and then drying. Before each mixture was prepared the forsterite

141   end-member was dried at 1000 °C for one hour and the water-bearing forsterite end-

142   member was dried overnight at 120 °C. This approach was also followed for the

143   preparation of starting mixtures in the system $MgSiO_3$-H_2O. In this case, an end-member

144   1:1 molar mixture of brucite and SiO_2, corresponding to a composition of $MgSiO_3$ with

145   15.2 wt% bulk H_2O, was initially prepared (Table 1). The dry end-member $MgSiO_3$ was

146   prepared from high purity oxides MgO and SiO_2 and the dry and hydrous end-members

147   were mixed in different mass proportions to obtain the compositions given in Table 1.

148   Once prepared, all final mixtures were stored in a furnace at 120 °C to limit the

149   adsorption of water.

150

151   Platinum or platinum/rhodium multi-chamber capsules were fabricated from 2 mm

152   diameter Pt or Pt/Rh ($Pt_{90}Rh_{10}$) rods cut into 1 mm long sections. The resulting discs were

153   spark eroded on one surface, obtaining rows of 4 to 6 chambers per disc with the

154   chambers being 0.25 mm in diameter and approximately 0.66 mm deep. Each chamber

155   was loaded with a different starting powder such that H_2O contents increased across the

156   row of chambers. Sample powders were packed into each chamber using a tungsten-

157   rhenium needle. When packed sufficiently the chambers remained full even when air was

158   blown over the surface. Blowing air removed extraneous sample powders from chambers

159   that had not yet been loaded. The Pt capsules were closed by placing a second Pt disc

160   0.25 mm thick on top of the chambers, which was held closed under pressure. When

161 Pt/Rh capsules were employed the open extremities of the chambers were closed by

162 placing on top 6 foils of Pt/Rh with total thickness of ~0.25 mm.

163

164 High pressure and high temperature experiments were carried out using a multianvil

165 apparatus installed at the Bayerisches Geoinstitut (BGI). The experiments were

166 performed in an 18/11 assembly, with an 18 mm edge length Cr_2O_3-doped MgO

167 octahedral pressure medium and 11 mm WC-anvil corner truncations. Experiments at 6

168 GPa were performed using a 500 tonne Walker-type multi anvil press and a 5000 tonne

169 Kawai-type multianvil press. The experiments at 13 GPa were carried out only with the

170 5000 tonne multianvil apparatus. The pressure calibration at 6 GPa was performed using

171 the $CaGeO_3$ garnet to perovskite phase transition (Ross et al, 1986) for the 500 tonne

172 multianvil apparatus, while the pressure calibration described by Frost et al. (2004) was

173 employed for the experiments performed with the 5000 tonne press. A stepped graphite

174 heater was used in the experiments at 6 GPa, while for those performed at 13 GPa a

175 stepped $LaCrO_3$ heater was employed. Temperatures during the experiments were

176 monitored using a $W_{97}Re_3$–$W_{75}Re_{25}$ (D type) thermocouple inserted within an alumina

177 sleeve. The thermocouple junction was in contact with the base of the spark eroded

178 capsules, ~0.5 mm from the sample chambers, with an estimated temperature uncertainty

179 of 50 °C (Frost et al., 2004). However, higher uncertainty (100 °C) is considered for

180 experiments where the thermocouple reading failed and temperature was determined

181 based on power-temperature calibrations. A 25 μm thick foil of rhenium was placed on

182 the top of the capsule in order to avoid direct contact between the capsule and the

183 thermocouple junction. The maximum temperature fluctuation during the experiments

184   was ± 5 ℃. The capsule was surrounded by MgO spacers and sleeves. Each experiment

185   was first pressurised over 4 hours then heated in ~15 minutes to target temperature where

186   it remained for up to 30 minutes depending on target temperature. Once completed, the

187   experiment was quenched by turning off the power supply to the graphite/LaCrO$_3$ heater,

188   and decompression was carried out over approximately 15 hours.

189

190   After each experiment, the Pt or Pt/Rh sample disk was recovered, mounted in epoxy and

191   polished in the absence of water. Due to the high porosity of the charges, impregnation

192   with either epoxy resin or superglue was often required in order to avoid loss of material

193   during the polishing. Once the samples were polished, phase identification and chemical

194   analyses were carried out using a JEOL-JXA-8200 electron microprobe (EMPA) at the

195   BGI. Conditions of 15 kV and 15 nA for the accelerating voltage and beam current,

196   respectively, were adopted in all the analyses, using a beam diameter of ~1 μm. Standards

197   for SiO$_2$ and MgO were forsterite and enstatite, respectively, and all the analyses were

198   processed following the ZAF corrections.

199

200   Raman spectroscopy was conducted on some of the experimental charges to confirm the

201   nature of the mineral phases produced. The analyses were performed using a LABRAM

202   Raman spectrometer installed at the BGI and operating with a He-Ne laser with 632 nm

203   red-line wavelength. Analyses were performed with a total of 3 spectrum collections and

204   an accumulation time of 15 seconds each.

205

206   **3. Results**

207 Sections of typical experimental runs are shown in Fig. 1. At both pressures of 6 and 13

208 GPa melts quenched to produce a fine intergrowth of crystals. However, crystals that

209 were solid phases during heating of the experiments were easily distinguished from the

210 quenched crystals based on their euhedral character and grain size. In some experiments

211 quenched areas with different grain sizes and crystallite shapes could be observed that

212 might be interpreted as separate coexisting liquids, or vapour (Fig. 1a). Given that the

213 H_2O contents of the charges are relatively low for fluid-saturated conditions to be

214 encountered (e.g. Mibe et al., 2002), it seems more likely that these differences in texture

215 result from local differences in nucleation and growth during quenching of the

216 experiments. All quench textures are consistent with an origin as H_2O-bearing melts

217 rather than aqueous fluids. This distinction is made based on the quench crystal density

218 compared to previous studies performed at lower temperatures where a sub-solidus

219 aqueous fluid phase was encountered (Mibe et al. 2002).

220

221 Sections were ground by hand to over half way through the sample chambers to verify

222 the absence of crystals in experiments interpreted to have encountered superliquidus

223 conditions. Continual checks were made during grinding to examine for crystals that

224 might not otherwise appear in the final section. Some samples were ground more than

225 80% through to ensure that no crystals were present in the charge. The small size of the

226 sample chambers should ensure that thermal gradients across the samples are minimal.

227 The large relative size of the metal capsule should also help to relax thermal gradients.

228 Based on measurements performed in similar assemblies using two pyroxene

229 thermometry (Brey et al., 1990), the thermal gradients within each chamber are estimated

230 to be <20 °C.

231

232 Several experiments were performed at the same conditions but with different heating

233 durations in order to assess H_2O loss from the Pt capsules during the experiments. Two

234 experiments loaded with the same starting mixtures were performed at 6 GPa and 1400

235 °C for 5 and 30 minutes, respectively, and in both cases the resulting assemblages in each

236 of the sample chambers were identical. At 13 GPa the same result was obtained in two

237 experiments performed at 1450 °C. These observations imply that significant loss of H_2O

238 does not occur in experiments with run durations up to 30 minutes at temperatures up to

239 1450 °C. However, it was observed that in some experiments performed at higher

240 temperatures (>1650 °C), run durations greater than 30 minutes led to substantial

241 crystallisation, likely due to H_2O loss from the Pt capsule. Therefore, experiments

242 performed above 1650 °C were held at target temperature for 5-20 minutes only.

243

244 **3.1 Experimental results at 6 GPa**

245 Experimental conditions and phase assemblages of the runs performed at 6 GPa for both

246 Mg_2SiO_4-H_2O and $MgSiO_3$-H_2O systems are summarized in Table 2. In the forsterite-

247 H_2O system, experiments were performed from 1250 to 1650 °C (Fig. 2). In some runs

248 performed at 1250 °C crystals of enstatite were also observed, possibly suggesting

249 incongruent melting at these conditions. However, this observation is not in agreement

250 with the experimental results of Inoue (1994), which indicate the transition from

251 congruent to incongruent melting of forsterite in the system Mg_2SiO_4-H_2O to occur

11

252 between 7.7 and 12 GPa. Rather than incongruent melting, the appearance of enstatite is

253 possibly due to slight variations of certain starting mixtures from the Fo-H_2O join, which

254 would be more visible at high degrees of crystallization. Our data suggest that the

255 invariant curve Fo + En = Liquid is passing very close to the fo-H_2O line and possibly

256 crossing it (Fig. 3), explaining the observed phase relations (Table 2). In experiments

257 conducted at temperatures above 1250 ℃, the run products contained either forsterite and

258 melt or melt only, implying congruent melting. The run with the highest H_2O content

259 (20.4 wt%) produced crystals in equilibrium with quenched melt at 1250 ℃, hence it had

260 not yet reached the liquidus temperature (Table 2). However, at temperatures higher than

261 1250 ℃, most experiments had one or more chambers that contained a supraliquidus

262 product that comprised only quenched melt. At 1400 ℃, for example, forsterite crystals

263 coexisting with melt were produced in charges with H_2O contents of 7.9, 9.7, 13.8 wt%,

264 but the run with 18.3 wt% H_2O contained only hydrous melt (Fig. 1b, Table 2). The

265 proportion of crystals in each of these runs decreases in agreement with the lever rule as

266 the crystal-melt region is crossed as a function of H_2O content in the system. No

267 interpretation of these proportions is made, however, as it may be inaccurate due to the

268 particular sample section obtained during polishing.

269

270 In the $MgSiO_3$-H_2O system, experiments were carried out from 1050 ℃ to 1650 ℃, with

271 starting mixtures containing up to 15.2 wt% H_2O (Table 2, Fig. 4). All run products

272 contained enstatite and melt or melt only, indicating that melting occurred congruently

273 over the entire temperature range. In one experiment (V704, Table 2) a tiny crystal of

274 forsterite was found as an inclusion in a large enstatite crystal, but this was most likely a

275 consequence of chemical inhomogeneity in the starting mixture. The enstatite liquidus is

276 bracketed at 1650 °C at ~10 wt% H_2O and at 1500 °C at ~15 wt% H_2O.

277

278 **3.2 Experimental results at 13 GPa**

279 Experimental conditions and phase assemblages observed at 13 GPa for both systems

280 Mg_2SiO_4-H_2O and $MgSiO_3$-H_2O are summarized in Table 3. Experiments were

281 performed between 1300 and 1900 °C. In the Mg_2SiO_4-H_2O system, forsterite was found

282 to melt incongruently to an assemblage containing enstatite, forsterite and hydrous melt

283 at temperatures below 1600 °C (Fig. 5). However, the congruent forsterite liquidus could

284 be bracketed at 1700 °C between 13.8 and 20.4 wt% H_2O and at 1900 ºC between 5 and

285 13.8 wt % H_2O (Table 3). At 1300 °C, for example, the formation of forsterite in

286 equilibrium with melt was observed at the highest bulk water contents (20.4 wt%), while

287 enstatite was also crystallized at lower bulk H_2O contents. This is possibly due to the fact

288 that the univariant Fo + En = Liquid curve has moved closer to the Fo-H_2O join and small

289 variations within the bulk composition causes enstatite to crystallize (Fig. 3). At 1500 °C,

290 the Mg_2SiO_4 plus 5 wt% H_2O starting mixture produced forsterite and melt along with

291 minute crystals of MgO (estimated to be <1 vol%). The lower temperature of this

292 experiment compared to others where MgO was not observed implies that the MgO

293 crystals most likely formed due to a slight inhomogeneity in the starting mixture, rather

294 than an incongruent melting reaction. As we do not observe the presence of MgO in any

295 other of the experiments it is likely that the Fo + Per = Liquid univariant curve crosses

296 the Fo-H_2O join at lower H_2O contents than studied (Fig 3), which can be then roughly

297 constrained using the study of Presnall and Walter (1993).

13

298

299   In the system $MgSiO_3$-H_2O, enstatite melted congruently at 1900 ℃ and the liquidus

300   curve was bracketed at this temperature between 4.3 and 10 wt% H_2O (Fig. 6). However,

301   in some of the experiments performed between 1300 and 1700 ℃, the formation of small

302   crystals of stishovite occurred along with enstatite and melt, in agreement with

303   observations of Yamada et al. (2004) at 13.5 GPa. The presence of stishovite may be due

304   to the fact that En + St + L univariant curve has moved near to the En-H_2O join, or even

305   crossed it (Fig. 3). This phase, however, was observed only as a minor component, ~2

306   vol%, and is, therefore, not expected to cause significant departures from the determined

307   phase relations. Additionally, the enstatite liquidus curve was bracketed at 1700 ℃

308   between 6.2 and 11.8 wt% H_2O. At 1600 °C, the most H_2O-rich charge (15.2 wt% H_2O)

309   produced an assemblage of enstatite plus melt, which constrains the minimum H_2O

310   concentration of the liquidus melt at this temperature.

311

312   **4. Discussion**

313

314   **4.1 Model for hydrous melting of Mg₂SiO₄ and MgSiO₃**

315   A number of studies have examined the melting point depression of silicate minerals as a

316   function of H_2O content in the melt using the cryoscopic equation (e.g. Silver and Stolper

317   1985; Medard and Grove, 2008; Hirschmann et al., 2009; Myhill et al., 2016). For

318   Mg_2SiO_4 at the liquidus, for example,

319

320     $$\ln a_{Mg_2SiO_4}^{melt} = \frac{-\Delta_m G^{\circ}}{RT} \qquad (1)$$

321

where $\Delta_m G^o$ is the standard state Gibbs free energy of melting of pure forsterite (see

Appendix) and $a_{Mg_2SiO_4}^{melt}$ is the activity of the Mg_2SiO_4 component in the binary Mg_2SiO_4-

H_2O melt. At temperatures below the pure forsterite melting point, $\Delta_m G^o$ can be

determined by integrating the entropy of melting of pure Mg_2SiO_4, $\Delta_m S^o$, between the

temperature of interest, T, and the anhydrous melting point, Tm. Assuming that $\Delta_m S^o$ is

constant with temperature, Eq. (1) becomes:

$$\ln a_{Mg_2SiO_4}^{melt} = \frac{\Delta_m S^o (T - T_m)}{RT}. \qquad (2)$$

The standard entropies of melting for Mg_2SiO_4 and $MgSiO_3$ solid phases have been

derived from calorimetric measurements at 1 bar (e.g. Navrotsky et al. 1989; Richet et al.,

1993) and expressions for $\Delta_m S^o$ at higher pressures can be determined from data on the

anhydrous melting curves combined with equations of state for solid and liquid Mg_2SiO_4

or $MgSiO_3$ (see Appendix).

Use of the cryoscopic equation requires a plausible relationship between the activity and

concentration of silicate species in the hydrous melt, which will depend on the H_2O

concentration in the melt and its dissolution mechanism. Empirical molecular mixing of

Mg_2SiO_4 or $MgSiO_3$ and H_2O does not produce a sufficient depression of the liquidus to

explain the experimental data and it has long been recognized that upon dissolution in

silicate melts H_2O dissociates into hydroxyl groups bonded to the silicate framework

15

343 (Burnham 1975, 1979, 1994; Stolper, 1982; Silver and Stolper, 1989; Zotov and Keppler,

344 1998), i.e.

345

346 $\quad$ $H_2O + O^{2-} = 2\ OH^-$. $\hfill (3)$
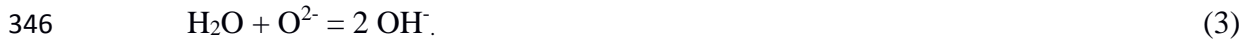
347

348 Spectroscopic analyses indicate that both molecular H_2O and OH^- groups are present in

349 silicate melts (e.g. Stolper, 1982, Dixon and Stolper, 1995), and their properties are

350 temperature-dependent (Nowak and Behrens, 1995; Zotov and Keppler, 1998). Silver and

351 Stolper (1985) proposed a thermodynamic model to describe the effects of H_2O

352 speciation on the activity of silicate melt components. They assumed that all three species

353 (H_2O, O^{2-} and OH^-) mix ideally following a homogeneous melt equilibrium (Eq. 3). The

354 activity of the silicate component, $a_{Mg_2SiO_4}^{melt}$, is related to the mole fraction of non-protonated

355 oxygen atoms in the melt, $X_{O^{2-}}^{melt}$, through the expression

356

357 $\quad$ $a_{Mg_2SiO_4}^{melt} = (X_{O^{2-}}^{melt})^r$ $\hfill (4)$

358

359 where r is the number of oxygen atoms available for protonation and mixing per formula

360 unit of silicate, with the chosen formula unit being consistent with the value of $\Delta_m S^o$.

361 Setting r=4 for Mg_2SiO_4 or 3 for $MgSiO_3$ implies that H can bond to any of the oxygen

362 atoms in the silicate melt structure.

363

364 The extent of H_2O dissociation in the silicate melt (Eq. 3) is described by the equilibrium

365 constant K,

366

$$K = \frac{\left(X_{OH^-}^{melt}\right)^2}{X_{H_2O}^{melt} X_{O^{2-}}^{melt}} \tag{5}$$

368

369 Following mass balance,

370

$$X_{H_2O^{tot}}^{melt} = X_{H_2O}^{melt} + 0.5 X_{OH^-}^{melt} \tag{6}$$

372

373 where $X_{H_2O^{tot}}^{melt}$ is the total mole fraction of H_2O in the silicate-H_2O melt. Solving Eqs. (5)

374 and (6) simultaneously, subject to the closure constraint

375

$$X_{H_2O}^{melt} + X_{OH^-}^{melt} + X_{O^{2-}}^{melt} = 1 \tag{7}$$

377

378 yields mole fractions of all three species in the hydrous melt. Substituting Eq. (5) and (6)

379 into Eq. (7) yields

380

$$X_{H_2O^{tot}}^{melt} = 1 - X_{O^{2-}}^{melt} + \frac{KX_{O^{2-}}^{melt} - \sqrt{\left(KX_{O^{2-}}^{melt}\right)^2 + 4KX_{O^{2-}}^{melt} - 4K\left(X_{O^{2-}}^{melt}\right)^2}}{4} \tag{8}$$

382

383 which is evaluated for the fraction of non-protonated oxygen atoms in the melt. The

384 corresponding activity of the silicate melt component is calculated from Eq. (4) and the

385 liquidus temperature is then defined by Eq. (2). In order to compare the results of the

17

386 model with experimental data, $X_{H_2O^{tot}}^{melt}$ can be converted to $w_{H_2O^{tot}}^{melt}$, the mass fraction of

387 H_2O dissolved in the melt using,

388

389
$$w_{H_2O^{tot}}^{melt} = \frac{X_{H_2O^{tot}}^{melt} M_{H_2O}}{X_{H_2O^{tot}}^{melt} M_{H_2O} + \left(1 - X_{H_2O^{tot}}^{melt}\right)\frac{M_{sil}}{r}} \tag{9}$$

390

391 where M_{H_2O} is the molar mass of water (18.015 g/mol) and M_{sil} is the molar mass of the

392 silicate formula unit.

393

4.1.1 Liquidus depression at 6 GPa

395 Fig. 2 shows the experimental results for the forsterite liquidus as a function of melt H_2O

396 content at 6 GPa compared to liquidus calculations using several limiting cases of the

397 thermodynamic model. The thermodynamic data used to determine the anhydrous

398 melting point of Mg_2SiO_4 and $\Delta_m S^o$ at the pressure and temperature of interest are listed

399 in Table A (see Appendix and Supplementary Material).

400

401 Three different curves for the Mg_2SiO_4 liquidus are shown calculated for different values

402 of the dissociation equilibrium constant, K. If all H_2O is completely dissociated to OH⁻ (K

403 $= \infty$), the experimental data at the lowest temperatures are in poor agreement with the

404 model as the experimental liquidus becomes less depressed at high H_2O contents. On the

405 other hand, if all H_2O is dissolved in the molecular form ($K = 0$), the predicted liquidus

406 curve is not in agreement with experimental data at any H_2O concentration. The change

407 in slope of the experimental liquidus implies that K is not constant over the range of

18

408 experimental temperatures, but must change from a high or infinite value (>50) above

409 1400 °C to <10 below 1300 °C, i.e. molecular H_2O becomes more important as the H_2O

410 saturated solidus is approached. Variations in K with temperature can be described using

411 the function,

412

413 $$\ln K = \frac{a}{T} + b,$$ (10)

414

415 which mimics the enthalpic and entropic contributions to K. The experimental data do not

416 provide sufficient constraints to determine the a and b coefficients in Eq. (10) uniquely

417 due to their high correlation. Values of $a \sim$ -7000 K and $b \sim$ 5.6 are in reasonable

418 agreement, however, with the data and their uncertainties. A different set, $a =$ -8000 K

419 and $b =$ 8, recently proposed for alkaline basalt by Lesne et al. (2011) based on

420 spectroscopic measurements would also just fit the experimental uncertainties, but start to

421 diverge at temperatures below 1300 °C. The experimental data can only be used to imply

422 a qualitative, strong dependence of K on temperature. Independent *in-situ* spectroscopic

423 data would be required to provide a more accurate estimate of this dependence.

424

425 Although the model is relatively simple, improvements that would provide a significantly

426 better fit to the experimental data are relatively limited, without making the model

427 completely empirical. For example, a slightly better agreement between the liquidus

428 curve and the experimental data at ~1450 °C can only be achieved by decreasing the

429 standard entropy of forsterite melting at 1 bar, which is already near the lower limit

430 derived from calorimetric studies (see Appendix). Non-ideal mixing can be included in

431   the model, however, a simple symmetric mixing parameter between the Mg_2SiO_4 and

432   H_2O components produces no significant improvement of the fit. In addition, such terms

433   have been shown to be unnecessary to describe the effect of H_2O on melting at lower

434   temperatures, where non-ideal effects should be even more important (Silver and Stolper,

435   1985).

436

437   We further compare our experimental results with the model of Tenner et al. (2012a),

438   which is based on the limiting case where all H_2O dissolves as OH^-. In Fig. 2, the liquidus

439   is calculated according to this model using the same thermodynamic data as above and

440   assuming $r = 4$ (random protonation of all oxygen atoms), which is analogous to using a

441   single-oxygen formula unit for the silicate end-member (Tenner et al. 2012a; their Eqs. 9

442   and 11). The predicted liquidus is substantially different from that obtained from the

443   Silver and Solper (1985) model with $K = \infty$, although both models should be equivalent

444   in describing the liquidus depression when H_2O dissolves completely as OH^-. The

445   difference arises in the conversion relationships for the mass fraction of H_2O by Silver

446   and Stolper (1985) and Tenner et al. (2012a). To bring these two models to numerical

447   consistency, the following relationship would have to be used to calculate the mole

448   fraction of OH^- in the melt from the H_2O mass fraction,

449

450   $$X_{OH^-}^{melt} = 2 \frac{w_{H_2O^{tot}}^{melt}/M_{H_2O}}{w_{H_2O^{tot}}^{melt}/M_{H_2O} + \left(100 - w_{H_2O^{tot}}^{melt}\right)/M_{sil}}, \qquad (11)$$

451

452   rather than the conversion equation proposed by Tenner et al. (2012a). The model of

453   Tenner et al. (2012a) has been found to quite accurately reproduce the liquidus of

454   experiments performed in natural complex systems when silicates are mixed on a 3-

455   oxygen formula basis. However, the model does not reproduce data on Mg_2SiO_4 at 6

456   GPa, regardless of the silicate molecular unit considered, providing an independent

457   confirmation that H_2O upon dissolution in silicate melt incompletely dissociates to OH^-.

458

459   A further complexity in the model would be to consider the possibility that not all of the

460   oxygen atoms in the melt structure are available for protonation but, for example, $r = 1$ or

461   2 per 4-oxygen formula unit (silicate polyhedron) due to local avoidance or ordering

462   principles. This consideration raises two issues, however. First, it would imply a

463   maximum limit for H_2O solubility in the melt, which appears to be not the case. Second,

464   if the number of oxygen sites, which are accessible for proton bonding became an

465   adjustable parameter and were allowed to change, for example, with the H_2O

466   concentration, the resulting fit parameters would be highly correlated with K. These

467   parameters cannot be meaningfully constrained without an independent estimate of K.

468   Therefore, the Silver and Stolper (1985) model with temperature-dependent speciation in

469   the melt supported by current estimates for $\Delta_m S^o$ of forsterite and the pressure-

470   temperature melting curve of anhydrous forsterite appears to provide an adequate and

471   well-constrained approximation of the experimental data.

472

473   In Fig. 4 experimental results bracketing the $MgSiO_3$-H_2O liquidus at 6 GPa are

474   compared with the same set of models as described above. The model that considers

21

475   complete dissociation to OH⁻ ($K = \infty$) agrees with experimental data at the highest

476   temperatures investigated (above 1600 °C). At lower temperatures, the experimental data

477   again imply a shallower liquidus slope that is not consistent with the complete

478   dissociation of H_2O into OH⁻. On the other hand, mixing with molecular H_2O only ($K =$

479   0) results in a liquidus curve far outside of the experimental uncertainties. A model that

480   considers variation of K with temperature (Eq. 10) fulfils the constraints imposed by the

481   experiments, although a large range of parameters in this equation can provide an

482   adequate fit to the data. The curve in Fig. 4 was calculated with values of a = -6000 K

483   and b = 4.5 with K decreasing from ~7 at 2100 °C to ~2 at 1300 °C. In addition, two

484   models from Tenner et al. (2012a) that assume mixing of silicate molecules with 1- and

485   3-oxygen formula units, respectively, are shown in Fig. 4. The model of Tenner et al.

486   (2012a) based on 1-oxygen per formula unit predicts values within the experimental

487   uncertainties. However, these authors find the best agreement with melting data using

488   natural peridotite composition when a 3-oxygen silicate molecule is assumed but, as

489   shown in Fig. 4, this is in poor agreement with the data in this simple $MgSiO_3$-H_2O

490   subsystem.

491

492   Both enstatite and forsterite melting experiments at 6 GPa can be described by Silver and

493   Stolper (1985) models that assume mixing of H on all silicate oxygen atoms and a

494   temperature-dependent dissociation of H_2O, which proceeds towards complete OH⁻

495   formation above ~1400 °C. It is interesting to note that the mass fraction (wt %) of H_2O

496   in the liquidus melt at a given temperature is nearly identical at 6 GPa for both $MgSiO_3$

497   and Mg_2SiO_4 over the entire temperature range.

498

4.1.2 Liquidus depression at 13 GPa

In Fig. 5 experiments bracketing the Mg_2SiO_4-H_2O liquidus at 13 GPa are shown and compared to the same models as described for the results at 6 GPa. The melting of pure Mg_2SiO_4 becomes incongruent above 10 GPa, with Mg_2SiO_4 reacting to produce MgO and melt at the solidus (Presnall and Walter, 1993). Upon the addition of H_2O to the system, melting becomes congruent between 1700-1900 °C (Table 3). For the purpose of modelling the forsterite liquidus, thermodynamic data for congruent Mg_2SiO_4 melting at lower pressures have been extrapolated using the melt model of de Koker and Stixrude (2009) to 13 GPa. Models using complete dissociation into OH$^-$ by Silver and Stolper (1985) with $K = \infty$ and by Tenner et al. (2012a) do not reproduce the experimental data (Fig. 5). The best agreement with the experimental liquidus is found for the limiting case of no dissociation, that is, mixing of molecular H_2O ($K = 0$ or 0.2). There are, however, larger inherent uncertainties in performing this evaluation at 13 GPa arising from the melting temperature assumed for anhydrous Mg_2SiO_4. Although the thermodynamic model of de Koker and Stixrude (2009) used here provides some theoretical justification for the extrapolation, the resulting dramatic change predicted in the H_2O speciation most probably arises from resulting inaccuracies in the temperature of metastable forsterite melting. By assuming an anhydrous melting temperature that is 250 °C higher than predicted by the anhydrous melting model, the temperature-dependent model for K calibrated at 6 GPa for Mg_2SiO_4 can be equally applied at 13 GPa. We conclude, therefore, that it is more likely that the anhydrous melting temperature is in error, than that there is a dramatic shift in H_2O speciation at high pressure. This highlights the

23

521 problems of examining melting point depression in incongruent systems, which are likely

522 to be even more complex for natural multicomponent systems such as mantle peridotite

523 melts.

524

525 For $MgSiO_3$, the liquidus depression at 13 GPa is consistent with the Silver and Stolper

526 (1985) model for nearly complete dissociation to OH^- in the melt (Fig. 6). While this is in

527 contrast to Mg_2SiO_4 at the same pressure, it is in better agreement with the experimental

528 results at 6 GPa. Introducing a temperature dependence to K is not justified by the data,

529 within the experimental uncertainties. A molecular H_2O model is far outside of the

530 experimental constraints, however, as is the model of Tenner et al. (2012a).

531

532 **4.2 The effect of pressure on liquidus depression due to H_2O in simple and complex**

533 **silicate systems**

534 The liquidus depression under hydrous conditions in comparison to the anhydrous

535 melting point is shown for both the $MgSiO_3$-H_2O and Mg_2SiO_4-H_2O systems at 6 and 13

536 GPa in Fig. 7. Experimental data of Kushiro et al. (1968) for $MgSiO_3$-H_2O at 1 GPa and

537 between 1375 and 1525 °C are used in order to provide an additional comparison; a value

538 of $K = 0.5$ in the Silver and Stolper (1985) formulation provides a good fit to these data.

539 For $MgSiO_3$, pressure enhances the influence of H_2O in depressing the melting

540 temperature in line with thermodynamic estimates for the entropy of fusion and the

541 anhydrous melting curve of $MgSiO_3$. The effect of pressure on the water-driven melting

542 point depression of $MgSiO_3$ is best explained by an increase in the dissociation of H_2O

543 with increasing pressure, with essentially no molecular H_2O being involved above 1400

544 °C, at pressures of 6 GPa and higher.

545

546 For the Mg_2SiO_4-H_2O binary, however, there is an apparent decrease in the effect of H_2O

547 on liquidus depression between 6 and 13 GPa. As discussed above this is most likely

548 caused by an underestimate in the metastable melting temperature of anhydrous Mg_2SiO_4,

549 which melts incongruently above 10 GPa. If the anhydrous melting temperature is

550 assumed to be 250 °C higher at 13 GPa, then the effect on liquidus depression is reversed.

551 This implies that the extrapolated melting curve for Mg_2SiO_4 is incorrect. The Silver and

552 Stolper (1985) model with values of K = ~0.2 at 2100 °C and approaching 0 at 1300 °C

553 successfully reproduce experimental data of Hodges (1974) at 3 GPa in the forsterite-H_2O

554 system. Data at 3 GPa show lower melting temperature depression in comparison to those

555 at 6 GPa, is in agreement with the pressure trend observed in the enstatite-H_2O system

556 and further suggesting a positive effect of pressure on melting temperature depression.

557

558 In Fig. 7, data for the liquidus depression due to H_2O for melts of natural peridotite

559 composition are shown from Tenner et al. (2012a) at 3.5 GPa and Novella and Frost

560 (2014) at 6 GPa. The depression of melting due to H_2O is much smaller for these

561 complex melts compared to either of the simple systems at the same pressure. This

562 difference is partly due the lower anhydrous liquidus temperatures of the natural

563 multicomponent melts. As indicated by Eq. (2) the magnitude of the liquidus depression

564 should increase with the anhydrous melting temperature, as observed in all experiments.

565 In Fig. 7 these data are fitted using a Silver and Stolper (1985) model with molar mass of

566 37 g/mol per single-oxygen formula unit and a $\Delta_m S^o = 0.4$ J/(K·g) (Tenner et al., 2012a;

567 Kojitani and Akaogi, 1997). A constant value of $\Delta_m S^o$ in Eq. (2) is assumed at all

568 pressures and temperatures and the anhydrous melting temperatures are taken from

569 Walter (1998). The best correspondence with experiments at 3.5 GPa requires a

570 temperature dependent value of K, which starts near unity close to the anhydrous melting

571 temperature but decreases to effectively zero below 1200 °C. Although there is only one

572 data point available at 6 GPa the depression of melting is consistent with a similar model

573 as at 3.5 GPa, with the only difference being the anhydrous melting temperature. The

574 Silver and Stolper (1985) model, therefore, implies a much smaller extent of H_2O

575 dissociation into OH^- and a greater proportion of molecular H_2O in multicomponent melts

576 when compared to simple systems. This difference may have several origins, however.

577 First, the value of $\Delta_m S^o$ employed for peridotite melt is poorly constrained as it is derived

578 from calorimetric measurements in the $CaO\text{-}MgO\text{-}Al_2O_3\text{-}SiO_2$ system at 1 bar (Kojitani

579 and Akaogi, 1997) and it may not suitably account for the effects of pressure and

580 composition. Second, it is possible that certain components present in the natural

581 peridotite melt compositions, such as Al_2O_3, cause a reduction in the effect of H_2O on the

582 configurational entropy of the melt. As a result of such distinct behaviour, the effect of

583 H_2O on melting in such simple systems may be quite far away from that in complex

584 mantle melts.

585

586 Although the justification as to how the melt OH^- mole fraction is calculated is somewhat

587 unclear in the model of Tenner et al. (2012a), particularly in relation to the Silver and

588 Stolper (1985) model, it is interesting to note that it does closely predict the liquidus

589 depression for complex peridotitic melts at both 3.5 and 6 GPa. The model is based on a

590 3-oxygen melt described by Eq. (11) and it predicts curves identical to those shown in

591 Fig. 7 using the Silver and Stolper (1985) model for the natural peridotite data at 3.5 and

592 6 GPa. Although only empirical in its nature, it tends to numerically mimic decreasing

593 protonation of the oxygen sites in the silicate melt structure, and it produces a good fit to

594 the natural multicomponent data with fewer adjustable parameters. As there seems to be

595 no clear justification to the way in which the OH^- mole fraction is derived in the Tenner et

596 al. (2012a) model, the predictive capacity may be a coincidence.

597

598 **4.2.1 Hydrous melts along adiabatic temperature gradient**

599 A number of seismic observations appear to show evidence for low shear wave velocities

600 at the base of the upper mantle above the 410 km discontinuity (e.g. Song et al., 2004;

601 Vinnik et al., 2009; Jasbinken et al., 2010; Tauzin et al., 2010). These observations have

602 been proposed to result from the presence of low degree volatile-bearing melts at these

603 depths (Bercovici and Karato, 2003). Assuming that the upper mantle has a constant H_2O

604 content, it might be possible to explain the visibility of H_2O induced melting at the base

605 of the upper mantle if pressure enhances melt productivity at these conditions. One way

606 that this might occur is if less H_2O were required to stabilise melts with increasing

607 pressure.

608

609 In Fig. 7 the speciation model of Silver and Stolper (1985) using a temperature-dependent

610 value of K varying between ~1 and 0 at 3.5 and 6 GPa is extrapolated to 13 GPa by

611 assuming an anhydrous melting temperature of 1900 °C at this pressure (Takahashi,

27

612   1986). The model by Tenner et al. (2012a) would predict an identical liquidus depression.

613   The results of this extrapolation are given in Fig. 8, which shows the H_2O content in

614    $MgSiO_3$, Mg_2SiO_4 and peridotite melts determined at upper mantle adiabatic

615   temperatures (potential temperature ~1350 °C).

616

617   With increasing pressure the amount of H_2O required to stabilize Mg_2SiO_4 melt along a

618   mantle adiabat increases quite substantially between 6 and 13 GPa. This means that for a

619   system with a fixed H_2O content, the percentage of melt will decrease towards conditions

620   of the base of an upper mantle. This effect would work in conjunction with an increase in

621   the forsterite-melt H_2O partition coefficient with pressure (see Hirschmann et al., 2009;

622   Novella et al., 2014), which would also act to decrease the percentage of melting for a

623   given bulk H_2O concentration. By contrast, the H_2O content of a $MgSiO_3$ melt appears to

624   actually decrease slightly between 6 and 13 GPa, which could in theory lead to an

625   increase in the percentage of melting for a fixed H_2O content. However, the decrease in

626   melt H_2O content is small and this effect would be counteracted by an increase in the

627   enstatite-melt partitioning coefficient with pressure, calculated from the literature (Rauch

628   and Keppler, 2002; Yamada et al., 2004; Withers and Hirschmann, 2007; Withers et al.,

629   2011) and melt H_2O content from this study. Peridotite melts are also predicted to require

630   more H_2O to be stable at higher pressures, although the H_2O concentrations tend to vary

631   very little towards the base of the upper mantle similar in fact to $MgSiO_3$. This analysis

632   indicates that there is no evidence for increasing melt productivity due to H_2O towards

633   the base of the Earth's upper mantle, although it has to be recognised that there is some

634   uncertainty as the results for peridotite are being extrapolated above 6 GPa.

28

635

636 In order for the proportion of hydrous melting to increase and therefore be seismically

637 more visible towards the base of the upper mantle, the bulk mantle at these conditions

638 would need to be significantly enriched in H_2O. Such a localized enrichment in H_2O at

639 this depth would require an effective fractionation process to maintain high H_2O

640 concentrations at this depth. Bercovici and Karato (2003) proposed that hydrous melts

641 formed under these conditions may be neutrally buoyant and, therefore, separate from the

642 upwelling mantle and concentrate to form a low-velocity zone. Such a separation will

643 depend on melt density, which in turn will depend on the melt H_2O concentration. Melt

644 density experiments by Matsukage et al. (2005) favour such a scenario, although their

645 H_2O concentrations (~6 wt%) are approximately 50 % of those estimated in this study for

646 natural peridotitic melts at the bottom of the upper mantle (Fig. 8). Following the density

647 systematics of Jing and Karato (2009), partial melts in equilibrium with peridotite at 13

648 GPa should be much less dense than the surrounding mantle if the H_2O contents in the

649 melt are close to those predicted here (Fig. 8).

650

659 support by the Czech Science Foundation Project Nr. 210/12/0986. We thank associate

660 editor Mike Toplis and Mike Walter and an anonymous reviewer for comments that

661 significantly improved the manuscript.

662

663 **Appendix: Thermodynamic relations and parameters**

664 The Mie-Grüneisen equations of state (EOS) were employed to determine the Gibbs

665 energy of melting ($\Delta_m G^o$) of forsterite and enstatite required for the cryoscopic equation

666 in the Mg_2SiO_4-H_2O and $MgSiO_3$-H_2O binaries. Expressions to define the Gibbs energy

667 for Mg_2SiO_4 and $MgSiO_3$ were taken from Stixrude and Lithgow-Bertelloni (2011) for

668 solids and from de Koker and Stixrude (2009) for liquids and are based on the

669 fundamental thermodynamic relation between the Helmholtz energy (F) and the Gibbs

670 energy:

671

672 $\quad G(P, T) = F(V, T) + PV,$ $\hfill$ (A.1)

673

674 where V is the volume, P is the pressure and T is the temperature. The Helmholtz energy

675 at elevated pressure and temperature is obtained by stepwise integration from ambient

676 conditions ($T_0 = 298.15$ K, $P_0 = 101325$ Pa) *via* isothermal compression at reference

677 temperature (c) and isochoric heating (th), which accounts for the effect of thermal

678 vibrations:

679

680 $\quad F(V, T) = F(P_0, T_0) + \Delta F_c(T_0) + \Delta F_{th}(V).$ $\hfill$ (A.2)

681

682 The contribution to the Helmholtz energy due to isothermal compression (ΔF_c) was

683 calculated from the third-order Birch-Murnaghan EOS (Murnaghan, 1937; Birch, 1947;

684 e.g. Poirier, 2000):

685

686
$$\Delta F_c(T_0) = 9K_0V_0\left[\frac{f^2}{2} + \frac{af^3}{3}\right].$$
(A.3)

687

688 The EOS is based on the finite strain theory, where the finite strain (f) and the factor a are

689 calculated as follows:

690

691
$$f = \frac{1}{2}\left[\left(\frac{V_0}{V}\right)^{2/3} - 1\right]$$
(A.4)

692

693 and

694

695
$$a = \frac{3}{2}\left(K_0' - 4\right).$$
(A.5)

696

697 In this formulation, K_0 and V_0 correspond to the bulk modulus and the volume,

698 respectively, at the reference pressure and temperature, and K'_0 is the first pressure

699 derivative of the bulk modulus at reference conditions. The volume (V) of the phase at the

700 pressure and temperature of interest was found in order to satisfy the following relation:

701

702
$$P = P_c + P_{th} ,$$
(A.6)

703

704 where

705

706
$$P_{\mathrm{c}} = 3K_0 f (2f+1)^{5/2} (1+fa)$$
(A.7)

707

708 The equations of state for thermal pressure (P_{th}) and calculation of the relevant

709 thermodynamic properties differ for liquid and solid phases. For the liquid phases, the

710 thermal pressure is defined by

711

712
$$P_{\mathrm{th}} = \frac{\gamma}{V} c_{\mathrm{V}} (T - T_0)$$
(A.8)

713

714 where c_{V} is the isochoric heat capacity, and γ, representing the Grüneisen parameter, is a

715 function of volume as follows

716

717
$$\gamma = \gamma_0 + \gamma' \left(\frac{V}{V_0} - 1 \right)$$
(A.9)

718

719 where γ_0 is the Grüneisen parameter at the reference conditions and γ' is its first

720 derivative with respect to the volume. The thermal contribution to the Helmholtz energy

721 (ΔF_{th}) of a liquid is then defined by:

722

723
$$\Delta F_{\text{th}}(V) = -S_0(T-T_0) - c_{\text{v}}\left[T\ln\left(\frac{T}{T_0}\right) - (T-T_0)\right] - c_{\text{v}}(T-T_0)\left[(\gamma_0 - \gamma')\ln\left(\frac{V}{V_0}\right) + (\gamma - \gamma_0)\right]$$

724 (A.10)

725 where S_0 is the standard entropy of the substance at a reference state chosen to be

726 consistent with literature data as described above (see Table A).

727

728 For the solid phases, a slightly different approach was used starting with the calculation

729 of the volume at the pressure and temperature of interest (V). The thermal pressure of the

730 solid phase was determined using an expression for the Debye thermal energy (E_{th}), that

731 is,

732

733
$$P_{\text{th}} = \frac{\gamma}{V}\left[E_{\text{th}}(V,T) - E_{\text{th}}(V,T_0)\right]$$
(A.11)

734

735 and, in this case, the Grüneisen parameter is calculated as

736

737
$$\gamma = \gamma_0\left(\frac{V}{V_0}\right)^{q_0},$$
(A.12)

738

739 where q_0 is a constant, and the thermal internal energy (E_{th}) is defined by the Debye

740 model for the lattice vibrational energy

741

742

743
$$E_{th} = 9nRT\left(\frac{T}{\theta}\right)^3 \int_0^t \frac{t^3}{e^t - 1}dt,$$
(A.13)

744

745 where R is the universal gas constant, n is the number of atoms per formula unit, $t = \theta/T$,

746 with the Debye temperature (θ) calculated as

747

748
$$\theta = \theta_0 e^{\frac{\gamma_0 - \gamma}{q_0}}.$$
(A.14)

749

750 The corresponding expression for the thermal Helmholtz energy (F_{th}) of the solid phases,

751 defined as the Debye approximation of the quasi-harmonic vibrational density of states, is

752 as follows:

753

754
$$F_{th}(V) = 9nRT\left(\frac{T}{\theta}\right)^3 \int_0^t \ln\left(1 - e^{-t}\right)t^2 dt.$$
(A.15)

755

756 The thermal contribution to the Helmholtz energy (ΔF_{th}) of the solid phases between the

757 reference temperature (T_0) and that of interest (T) at the constant volume of interest (V), is

758 found by difference:

759

760
$$\Delta F_{th}(V) = F_{th}(V,T) - F_{th}(V,T_0).$$
(A.16)

761

762 The thermodynamic properties employed in the calculations of the Gibbs energy for solid

763 and liquid Mg_2SiO_4 and $MgSiO_3$ are summarized in Table A and are based on previous

764 compilations by de Koker and Stixrude (2009) and Stixrude and Lithgow-Bertelloni

765 (2011) for liquid and solid phases, respectively. The Helmholtz energy for liquid

766 substances at reference conditions (F_0) was empirically calculated from the room

767 pressure melting temperatures as explained by Liebske and Frost (2012). The reference

768 state volumes (V_0) and entropies (S_0) for the liquid end-members were slightly altered

769 compared to those reported by de Koker and Stixrude (2009) in order to obtain better

770 agreement with the experimental melting temperatures and to be consistent with

771 calorimetric data for the enthalpy of melting of $MgSiO_3$ and Mg_2SiO_4 (Navrotsky et al.,

772 1989; Richet et al., 1993). Specifically, the thermodynamic data of Mg_2SiO_4 liquid of de

773 Koker and Stixrude (2009) had to be modified such that the value of $\Delta_m S^o$ for forsterite at

774 1 bar was consistent with 52.7 J/(K·mol) proposed by Navrotsky et al. (1989). This is at

775 the lower end of the range of values reported in the literature, which vary from 70 to 47.5

776 J/(K·mol) (Bottinga, 1985; Navrotsky et al., 1989; Richet et al., 1993; Tangeman et al.,

777 2001). Values for the standard heat capacity and volume of Mg_2SiO_4 liquid were then

778 also adjusted to bring the model into agreement with experimental data on the melting

779 curve of Mg_2SiO_4 (Davis and England, 1964; Kato and Kumazawa, 1985; Presnall and

780 Walter, 1993).

781

782 **References**

783 Balta J.B., Asimow P.D. and Mosenfelder J.L. (2011) Hydrous, low-carbon melting of

784   garnet peridotite, *J. Petrol.* **52**, 2079–2105.

785 Bercovici D. and Karato S.-I. (2003) Whole-mantle convection and the transition-zone

786   water filter. *Nature* **425**, 39–44.

787 Brey G.P., Köhler T. and Nickel K.G. (1990) Geothermobarometry in four-phase

788   lherzolites I. Experimental Results from 10 to 60 kb. *J. Petrol.* **31**, 1313–1352.

789 Birch F. (1947) Finite elastic strain of cubic crystals. *Phys. Rev.* **71**, 809–824.

790 Bottinga Y. (1985) On the isothermal compressibility of silicate liquids at high pressure.

791   *Earth Planet. Sci. Lett.* **74**, 350–360.

792 Brooker R., Holloway J. and Hervig R. (1998) Reduction in piston cylinder experiments:

793   the detection of carbon infiltration into platinum capsules. *Am. Mineral.* **83**, 985-

794   994.

795 Burnham C.W. (1975) Water and magmas; a mixing model. *Geochim. Cosmochim. Acta*

796   **39**, 1077–1084.

797 Burnham, C.W. (1979) The importance of volatile constituents. In: *The Evolution of the*

798   *Igneous Rocks* (ed. H.S. Jr. Yoder). Princeton Univ. Press, Princeton, NJ. pp. 439–

799   482.

800 Burnham, C.W. (1994) Development of the Burnham model for prediction of H_2O

801   solubility in magmas. In: *Volatiles in Magmas* (eds. M.R. Carroll and J.R.

802   Holloway). Reviews in Mineralogy **30**, Mineralogical Society of America,

803   Washington D.C.

804 Dalton, J.A. and Presnall, D.C. (1997) No liquid immiscibility in the system $MgSiO_3$-

805   SiO_2 at 5.0 GPa. *Geochim. Cosmochim. Acta* **61**, 2367–2373.

806 Davis B.T.C. and England J.R. (1964) The melting of forsterite up to 50 kilobars. *J.*

807   *Geophys. Res.* **69**, 1113–1116.

808 de Koker N. and Stixrude L. (2009) Self-consistent thermodynamic description of silicate

809   liquids, with application to the shock melting of MgO periclase and $MgSiO_3$

810   perovksite. *Geophys. J. Internat.* **178**, 162–179.

811 Dixon J.E. and Stolper E.M. (1995) An experimental study of water and carbon dioxide

812   solubilities in mid-ocean ridge basaltic liquids. Part II: Applications to degassing.

813   *J. Petrol.*, **36**, 1633–1646.

814 Erlank E.J., Waters F.G., Hawkesworth C.J. Haggerty S.E., Allsopp H.L., Rickard R.S.

815   and Menzies M. (1987) Evidence for mantle metasomatism in peridotite nodules

816   from Kimberly pipes, South Africa. In: *Mantle Metasomatism* (eds. M.A. Menzies

817   and C.J. Hawkesworth). Academic Press, London, pp. 313–361.

818 Frost D.J., Poe B.T., Tronnes R.G., Liebske C., Duba A. and Rubie D.C. (2004) A new

819   large-volume multianvil system. *Phys. Earth Planet. Int.* **143–144**, 507–514.

820 Gaetani G.A. and Grove T.L. (1998) The influence of water on melting of mantle

821   peridotite. *Contrib. Mineral. Petrol.* **131**, 323–346.

822 Hirose K. and Kawamoto T. (1995) Hydrous partial melting of lherzolite at 1 GPa: the

823   effect of H_2O on the genesis of basaltic magmas. *Earth Planet. Sci. Lett.* **133**,

824   463–473.

825 Hirschmann M.M., Tenner T., Aubaud C. and Withers A.C. (2009) Dehydration melting

826   of nominally anhydrous mantle: The primacy of partitioning. *Phys. Earth Planet.*

827   *Int.* **176**, 54–68.

828 Hodges F.N. (1973) Solubility of H_2O in forsterite melt at 20 kbar. *Carnegie Inst.*

829   *Washington Yearb.* **72**, 495–497.

830   Hodges F.N. (1974) The solubility of H_2O in silicate melts. *Carnegie Inst. Washington*

831   *Yearb.* **73**, 251–255.

832   Inoue T. (1994) Effect of water on the melting phase-relations and melt composition in

833   the system Mg_2SiO_4-$MgSiO_3$-H_2O up to 15 GPa. *Phys. Earth Planet. Int.* **85**,

834   237–263.

835   Jasbinsek, J.J., Dueker, K.G. and Hansen, S.M. (2010) Characterizing the 410 km

836   discontinuity low-velocity layer beneath LA RISTRA array in the North American

837   Southwest. *Geochem. Geophys. Geosys.* **11**, doi:10.1029/2009GC002836.

838   Jing Z. and Karato S-I. (2009) The density of volatile bearing melts in the Earth's deep

839   mantle: The role of chemical composition. *Chem. Geol.* **262**, 100–107.

840   Kato T. and Kumazawa M. (1985) Melting and phase relations in the system Mg_2SiO_4-

841         $MgSiO_3$ at 20 GPa under hydrous conditions. *J. Geophys. Res.* **91**, 9351–9355.

842   Kawamoto T. and Holloway J.R. (1997) Melting temperature and partial melt chemistry

843   of H_2O-saturated mantle peridotite to 11 GPa. *Science* **276**, 240–243.

844   Kojitani H. and Akaogi M. (1997) Melting enthalpies of mantle peridotite: calorimetric

845   determinations in the system CaO-MgO-Al_2O_3,-SiO_2 and application to magma

846   generation. *Earth Planet Sci. Lett.* **153**, 209–222.

847   Kushiro I. (1972) Effect of water on the composition of magmas formed at high

848   pressures. *J. Petrol.* **13**, 311–334.

849   Kushiro I. and Yoder H.S.Jr. (1969) Melting of forsterite and enstatite at high pressures

850   and hydrous conditions. *Carnegie Inst. Washington Yearb.* **67**, 153–158.

851   Kushiro I., Yoder H.S.Jr. and Nishikawa, M. (1968) Effect of water on the melting of

852   enstatite. *Geol. Soc. Am. Bull.* **79**, 1685–1692.

853 Lambert I. B. and Wyllie P. J. (1970) Low-velocity zone of the Earth's mantle; incipient

854   melting caused by water. *Science* **169**, 764–766.

855 Lesne P., Scaillet B., Pichavant M., Iacono-Marziano G. and Beny J.M. (2011) The H_2O

856   solubility of alkali basaltic melts: an experimental study. *Contrib. Mineral. Petrol.*

857   **162**, 133–151.

858 Liebske C. and Frost D.J. (2012) Melting phase relations in the $MgO–MgSiO_3$ system

859   between 16 and 26 GPa: Implications for melting in Earth's deep interior. *Earth*

860   *Planet Sci. Lett.* **345–348**, 159–170.

861 Liu X., O' Neill H.St.C., and Berry A.J. (2006) The effects of small amounts of H_2O, CO_2

862   and Na_2O on the partial melting of spinel lherzolite in the system CaO-MgO-

863   Al_2O_3-SiO_2±H_2O±CO_2±Na_2O at 1.1 GPa. *J. Petrol.* **47**, 409–434.

864 Luth R.W. (1993) Melting in the Mg_2SiO_4-H_2O system at 3 to 12 GPa. *Geophys. Res. Let.*

865   **20**, 233–235.

866 Matsukage K.N., Jing Z. and Karato S-I. (2005) Density of hydrous silicate melt at the

867   conditions of Earth's deep upper mantle. *Nature* **438,** 488–491.

868 Médard E. and Grove T.L. (2008) The effect of H_2O on the olivine liquidus of basaltic

869   melts: experiments and thermodynamic models. *Contrib. Mineral. Petrol*. **155**,

870   417–432.

871 Menzies M.A. and Hawkesworth C.J. (1987) *Mantle metasomatism*. Academic press,

872   London.

873 Mibe K., Fujii T. and Yasuda M. (2002) Composition of acqueous fluid coexisting with

874   mantle minerals at high pressure and its bearing on the differentiation of the

875   Earth's mantle. *Geochim. Cosmochim. Acta* **66**, 2273–2285.

876   Mierdel K., Keppler H., Smyth J.R. and Langenhorst F. (2007) Water solubility in

877   aluminous orthopyroxene and the origin of Earth's asthenosphere. *Science* **315**,

878   364-368.

879   Murnaghan, F. D. (1937) Finite deformations of an elastic solid. *Amer. J. Math.* **49**, 235–

880   260.

881   Myhill, R., Frost, D.J. and Novella, D. (2016) Hydrous melting and partitioning in and

882   above the mantle transition zone: insights from water-rich $MgO\text{-}SiO_2\text{-}H_2O$

883   experiments.   *Geochim.*   *Cosmochim.*   *Acta,*

884   http://dx.doi.org/10.1016/j.gca.2016.05.027.

885   Mysen B.O. and Boettcher A.L. (1975) Melting of hydrous mantle I. Phase relations of

886   natural peridotite at high pressures and temperatures with controlled activities of

887   water, carbon dioxide, and hydrogen, *J. Petrol.* **16**, 520–548.

888   Navrotsky A., Ziegler D., Oestrike R. and Maniar P. (1989) Calorimetry of silicate melts

889   at 1773 K - measurement of enthalpies of fusion and of mixing in the systems

890   diopside-anorthite-albite and anorthite-forsterite. *Contrib. Mineral. Petrol.* **101**,

891   122–130.

892   Novella D. and Frost D.J. (2014) The composition of hydrous partial melts of garnet

893   peridotite at 6 GPa: implications for the origin of group II kimberlites. *J. Petrol.*

894   **5**, 2097–2124.

895   Novella D., Frost D.J., Hauri E.H., Bureau H., Raepsaet C. and Roberge M. (2014) The

896   distribution of water between nominally anhydrous peridotite and melts in the

897   Earth's upper mantle. *Earth Planet Sci. Lett.* **400**, 1–13.

898 Nowak M. and Behrens H. (1995) An in situ near infrared spectroscopic study of water

899   speciation in haplogranitic glasses and melts. *Fifth Silicate Melt Work-shop*

900   *Program and Abstracts*, La Petite Pierre, France.

901 Pamato M., Myhill, R., Boffa Ballaran T., Frost D.J., Heidelbach F. and Miyajima N.

902   (2015) Lower-mantle water reservoir implied by the extreme stability of a

903   hydrous aluminosilicate. *Nature Geoscience* **8**, 75–79.

904 Poirier J.P. (2000) Introduction to the physics of the Earth interior. 2nd ed, Cambridge

905   University Press, Cambridge.

906 Presnall D.C. and Walter M.J. (1993) Melting of forsterite, Mg_2SiO_4, from 9.7 to 16.5

907   GPa. *J. Geophys. Res.* **98**, 19777–19783.

908 Rauch, M. and Keppler, H. (2002). Water solubility in orthopyroxene. *Contrib. Mineral.*

909   *Petrol.* **143**, 525–536.

910 Richet P., Robie R.A. and Hemingway B.S. (1993) Entropy and structure of silicate

911   glasses and melts. *Geochim. Cosmochim. Acta* **57**, 2751–2766.

912 Ross N.L., Akaogi M., Navrotsky A., Susaki J., and McMillan P. (1986) Phase

913   transformations among $CaGeO_3$ polymorphs (wollastonite, garnet, and perovskite

914   structures): studies by high-pressure synthesis, high-temperature calorimetry and

915   vibrational spectroscopy and calculation. *J. Geophys. Res.* **91**, 4601–1696.

916 Schmandt B., Jacobsen S.D., Becker T.W., Liu Z. and Dueker K.G. (2014) Dehydration

917   melting at the top of the lower mantle. *Science* **344**, 1265–1268.

918 Silver L.A. and Stolper E.M. (1985) A thermodynamic model for hydrous silicate melts.

919   *J. Geol.* **93**, 161–178.

920 Silver L.A. and Stolper E.M. (1989) Water in albitic glasses. *J. Petrol.* **30**, 667–709.

Sokol A.G., Kupriyanov I.N., Palyanov Y.N., Krunk A.N. and Sobolev N.V. (2013) Melting experiments on the Udachnaya kimberlite at 6.3-7.5 GPa: Implications for the role of H_2O in magma generation and formation of hydrous olivine. *Geochim. Cosmochim. Acta* **101**, 133–155.

Song, A.T-R., Helmberger, D.V. and Grand, S.P. (2004) Low-velocity zone atop the 410-km seismic discontinuity in the northwestern United States. *Nature* **427**, 530–533.

Stixrude L. and Linthgow-Bertelloni C. (2011) Thermodynamics of mantle minerals − II. Phase equilibria. *Geophys. J. Int.* **184**, 1180–1213.

Stolper E. (1982) Water in silicate glasses: an infrared spectroscopy study. *Contrib. Mineral. Petrol.* **81**, 1–17.

Takahashi E. (1986) Melting of dry peridotite KLB-1 up to 14 GPa: implications on the origin of peridotitic upper mantle. *J. Geophys. Res.* **91**, 9367–9382.

Tangeman J.A., Lange R., and Forman L. (2001) Ferric-ferrous equilibria in K_2O-FeO-Fe_2O_3-SiO_2 melts. *Geochim. Cosmochim. Acta* **65** 1809–1819.

Tatsumi Y., Hamilton D.L. and Nesbitt R.W. (1986) Chemical characteristics of fluid phase released from a subducted lithosphere and origin of arc magmas: Evidence from high-pressure experiments and natural rocks. *J. Volcan. Geotherm. Res.* **29**, 293–309.

Tauzin B., Debayle E. and Wittlinger G. (2010) Seismic evidence for a global low-velocity layer within the Earth's upper mantle. *Nature Geoscience* **3**, 718–721.

Tenner T.J., Hirschmann M.M. and Humayun M. (2012a) The effect of H_2O on partial melting of garnet peridotite at 3.5 GPa. *Geochem. Geophys. Geosys.* **13**, doi:10.1029/2011GC003942.

944   Tenner, T.J., Hirschmann, M.M., Withers, A.C. and Ardia, P. (2012b) H_2O storage

945   capacity of olivine and low-Ca pyroxene from 10 to 13 GPa: consequences for

946   dehydration melting above the transition zone. *Contrib. Mineral. Petrol.* **163**,

947   297–316.

948   Vinnik, L., Oreshin, S., Kosarev, G., Kiselev, S. and Makeyeva, L. (2009) Mantle

949   anomalies beneath southern Africa: evidence from seismic S and P receiver

950   functions. *Geophys. J. Int.* **179**, 279–298.

951   Walter M.J. (1998) Melting of garnet peridotite and the origin of komatiite and depleted

952   Lithosphere. *J. Petrol.* **39**, 29–60.

953   Withers, A.C. and Hirschmann, M.M. (2007) H_2O storage capacity of $MgSiO_3$ clino-

954   enstatite at 8–13 GPa, 1100–1400 °C. *Contrib. Mineral. Petrol.* **154**, 663–674.

955   Withers, A.C., Hirschmann, M.M. and Tenner, T. (2011) The effect of Fe on olivine H_2O

956   storage capacity: consequences for H_2O in the Martian mantle. Am. Mineral 96,

957   1039–1053.

958   Yamada A., Inoue T. and Irifune T. (2004) Melting of enstatite from 13 to 18 GPa under

959   hydrous conditions. *Phys. Earth Planet. Int.* **147**, 45–56.

960   Zotov N. and Keppler H. (1998) The influence of water on the structure of hydrous

961   sodium tetrasilicate glasses. *Am. Mineral.* **83**, 823–834.

962

963   **Figure captions**

964   **Fig. 1**: Backscattered electron (BSE) images of experiments performed at 6 GPa in the

965   Mg_2SiO_4-H_2O system. The bright material is the Pt capsule. Grey crystals (50 to 100 μm

966   across) of forsterite can be easily distinguished from the fine grain quenched melt. (**a**):

967   figure corresponds to experiment V649 (Table 2) where in order from left to right are

968   sample chambers containing starting mixtures of Mg_2SiO_4 plus 5, 10, 15 and 20.4 wt%

969   H_2O in the bulk. The third chamber from the left shows two quench textures in the same

970   charge with different fibrous grain sizes, likely formed due to differences in nucleation

971   and crystal growth (see text). (**b**): BSE image of experiment V660 (Table 2) where, from

972   left to right, starting mixtures of Mg_2SiO_4 with 7.9, 9.7, 13.8 and 18.3 wt% H_2O (bulk)

973   were employed.

974   **Fig. 2**: Phase diagram of the Mg_2SiO_4-H_2O system at 6 GPa showing experimental data

975   and models for the liquidus curves (described in the text). Data points determined in this

976   study are displayed by black and grey symbols (Table 2) while data from Luth (1993) at 6

977   GPa and Inoue (1994) at 5.5 GPa are shown by blue and green symbols, respectively.

978   Data from Luth (1993) and Inoue (1994) were determined for bulk compositions of

979   Mg_2SiO_4 plus 20.4 wt% H_2O but are plotted at slightly higher H_2O content to aid

980   visibility. The liquidus at approximately 20 wt% H_2O is ~200 °C lower than reported by

981   Inoue et al. (1994) at 5.5 GPa but is in agreement, within uncertainty, with the data of

982   Luth (1993) at 6 GPa. The plotted liquidus curves are all constrained by the dry melting

983   temperature of forsterite at 6 GPa reported by Kato and Kumazawa (1985). Details

984   regarding the different curves are reported in the text. Uncertainties of 1 wt% in the melt

985   composition and 50-100 °C for the temperature of the experiments (see text) are

986   displayed by the error bars.

987   **Fig. 3**: Indicative ternary phase diagrams in the system MgO-SiO_2-H_2O. Phase relations

988   are tentatively constrained at 6 (top) and 13 (bottom) GPa by the experimental results

989   reported in this study and the literature. Starting compositions in the forsterite-H_2O and

990 enstatite-H_2O joins are plotted as black circles, on a molar basis. Fo: forsterite; En:

991 enstatite; Per: periclase; St: stishovite; L: liquid (or melt). The dashed line indicates the

992 Fo + En = L reaction curve while the dotted lines show the possible location of the Fo +

993 Per = L (toward MgO corner) and En + St = L (toward SiO_2 corner) curves.

994 **Fig. 4**: The depression of the $MgSiO_3$ liquidus curve at 6 GPa as a function of melt H_2O

995 content. Data points determined in this study (Table 2) are displayed by black symbols

996 while green symbols are from Inoue (1994), plotted at slightly higher H_2O content to aid

997 visibility. Uncertainties of 1 wt% in the melt composition and 50-100 °C for the

998 temperature of the experiments (see text) are displayed by the error bars. Curves

999 describing the liquidus determined by different models as described in the text are also

1000 shown. The liquidus curves are all constrained by the dry melting temperature of enstatite

1001 at 6 GPa reported by Kato and Kumazawa (1985).

1002 **Fig. 5**: Melting phase relations in the Mg_2SiO_4-H_2O system at 13 GPa. Uncertainties of 1

1003 wt% in the melt composition and 50-100 °C for the temperature of the experiments (see

1004 text) are displayed. The dry melting temperature of forsterite at 13 GPa was calculated to

1005 be 2200 °C by extrapolation of the equations of state of de Koker and Stixrude (2009).

1006 **Fig. 6**: The melting phase relations in the $MgSiO_3$-H_2O system at 13 GPa. Uncertainties

1007 of 1 wt% in the melt composition and 50-100 °C for the temperature of the experiments

1008 (see text) are displayed. The dry melting temperature of enstatite at 13 GPa was

1009 calculated to be 2250°C using the model of de Koker and Stixrude (2009). Values of a = -

1010 8000 K and b = 8 were employed in the calculation of constant K (red line).

1011 **Fig. 7:** The depression in the hydrous melting temperature as a function of H_2O for

1012 $MgSiO_3$-H_2O (black lines), Mg_2SiO_4-H_2O (green lines) and natural (blue lines) melt

1013 compositions between 1 and 13 GPa. Hydrous garnet peridotite melt compositions are

1014 from Tenner et al. (2012a) at 3.5 GPa (red dots) and Novella and Frost (2014) at 6 GPa

1015 (grey square). The blue curves are fitted to these data, as described in the text.

1016 **Fig. 8:** Melt H_2O contents as a function of pressure determined at 3.5, 6 and 13 GPa and

1017 at temperatures corresponding to a mantle adiabat (1350 °C, 1400 °C and 1500 °C,

1018 respectively). Peridotite data are taken from the curves shown in Fig. 7.